

STED with wavelengths closer to the emission maximum

Giuseppe Vicidomini,^{1,3} Gael Moneron,¹ Christian Eggeling,¹ Eva Rittweger,^{1,2} and Stefan W. Hell^{1,2,*}

¹Department of NanoBiophotonics, Max Planck Institute for Biophysical Chemistry, Am Fassberg 11, 37077 Göttingen, Germany

²German Cancer Research Center/BioQuant, Im NeuenheimerFeld 267, 69120 Heidelberg, Germany

³Currently with the Department of Nanophysics, Istituto Italiano di Tecnologia, Via Morego 30, 16163 Genoa, Italy
*shell@gwdg.de

Abstract: In stimulated emission depletion (STED) nanoscopy the wavelength of the STED beam is usually tuned towards the red tail of the emission maximum of the fluorophore. Shifting the STED wavelength closer to the emission peak, i.e. towards the blue region, favorably increases the stimulated emission cross-section. However, this blue-shifting also increases the probability to excite fluorophores that have remained in their ground state, compromising the image contrast. Here we present a method to exploit the higher STED efficiency of blue-shifted STED beams while maintaining the contrast in the image. The method is exemplified by imaging immunolabeled features in mammalian cells with an up to 3-fold increased STED efficiency compared to that encountered in standard STED nanoscopy implementations.

©2012 Optical Society of America

OCIS codes: (180.2520) Fluorescence microscopy; (350.5730) Resolution.

References and links

1. E. Abbe, *Gesammelte abhandlungen* (G. Fischer, Jena, 1904).
2. S. W. Hell, "Microscopy and its focal switch," *Nat. Methods* **6**(1), 24–32 (2009).
3. S. W. Hell, "Far-field optical nanoscopy," *Science* **316**(5828), 1153–1158 (2007).
4. B. Huang, H. Babcock, and X. Zhuang, "Breaking the diffraction barrier: super-resolution imaging of cells," *Cell* **143**(7), 1047–1058 (2010).
5. S. W. Hell and J. Wichmann, "Breaking the diffraction resolution limit by stimulated emission: stimulated-emission-depletion fluorescence microscopy," *Opt. Lett.* **19**(11), 780–782 (1994).
6. T. A. Klar, S. Jakobs, M. Dyba, A. Egner, and S. W. Hell, "Fluorescence microscopy with diffraction resolution barrier broken by stimulated emission," *Proc. Natl. Acad. Sci. U.S.A.* **97**(15), 8206–8210 (2000).
7. V. Westphal, S. O. Rizzoli, M. A. Lauterbach, D. Kamin, R. Jahn, and S. W. Hell, "Video-rate far-field optical nanoscopy dissects synaptic vesicle movement," *Science* **320**(5873), 246–249 (2008).
8. C. Eggeling, C. Ringemann, R. Medda, G. Schwarzmann, K. Sandhoff, S. Polyakova, V. N. Belov, B. Hein, C. von Middendorff, A. Schönle, and S. W. Hell, "Direct observation of the nanoscale dynamics of membrane lipids in a living cell," *Nature* **457**(7233), 1159–1162 (2009).
9. J. B. Ding, K. T. Takasaki, and B. L. Sabatini, "Supraresolution imaging in brain slices using stimulated-emission depletion two-photon laser scanning microscopy," *Neuron* **63**(4), 429–437 (2009).
10. B. R. Rankin, G. Moneron, C. A. Wurm, J. C. Nelson, A. Walter, D. Schwarzer, J. Schroeder, D. A. Colón-Ramos, and S. W. Hell, "Nanoscopy in a living multicellular organism expressing GFP," *Biophys. J.* **100**(12), L63–L65 (2011).
11. S. W. Hell and M. Kroug, "Ground-state depletion fluorescence microscopy, a concept for breaking the diffraction resolution limit," *Appl. Phys. B* **60**(5), 495–497 (1995).
12. S. Bretschneider, C. Eggeling, and S. W. Hell, "Breaking the diffraction barrier in fluorescence microscopy by optical shelving," *Phys. Rev. Lett.* **98**(21), 218103 (2007).
13. S. W. Hell, "Toward fluorescence nanoscopy," *Nat. Biotechnol.* **21**(11), 1347–1355 (2003).
14. M. Hofmann, C. Eggeling, S. Jakobs, and S. W. Hell, "Breaking the diffraction barrier in fluorescence microscopy at low light intensities by using reversibly photoswitchable proteins," *Proc. Natl. Acad. Sci. U.S.A.* **102**(49), 17565–17569 (2005).

15. T. Grotjohann, I. Testa, M. Leutenegger, H. Bock, N. T. Urban, F. Lavoie-Cardinal, K. I. Willig, C. Eggeling, S. Jakobs, and S. W. Hell, "Diffraction-unlimited all-optical imaging and writing with a photochromic GFP," *Nature* **478**, 204–208 (2011).
16. K. I. Willig, B. Harke, R. Medda, and S. W. Hell, "STED microscopy with continuous wave beams," *Nat. Methods* **4**(11), 915–918 (2007).
17. M. Leutenegger, C. Eggeling, and S. W. Hell, "Analytical description of STED microscopy performance," *Opt. Express* **18**(25), 26417–26429 (2010).
18. J. R. Moffitt, C. Osseforth, and J. Michaelis, "Time-gating improves the spatial resolution of STED microscopy," *Opt. Express* **19**(5), 4242–4254 (2011).
19. G. Vicidomini, G. Moneron, K. Y. Han, V. Westphal, H. Ta, M. Reuss, J. Engelhardt, C. Eggeling, and S. W. Hell, "Sharper low-power STED nanoscopy by time gating," *Nat. Methods* **8**(7), 571–573 (2011).
20. O. G. Peterson, J. P. Webb, W. C. McColgin, and J. H. Eberly, "Organic dye laser threshold," *J. Appl. Phys.* **42**(5), 1917–1928 (1971).
21. E. Rittweger, B. R. Rankin, V. Westphal, and S. W. Hell, "Fluorescence depletion mechanisms in super-resolving STED microscopy," *Chem. Phys. Lett.* **442**(4-6), 483–487 (2007).
22. A. Giske, "CryoSTED microscopy: A new spectroscopic approach for improving the resolution of STED microscopy using low temperature," PhD-Thesis (Ruperto-Carola University of Heidelberg, Heidelberg, 2007).
23. S. W. Hell and A. Schoenle, "Nanoscale resolution in far-field fluorescence microscopy," in *Science of microscopy*, P. W. Hawkes and J. C. H. Spence, eds. (2007), Chap. 12.
24. E. Auksorius, B. R. Boruah, C. Dunsby, P. M. P. Lanigan, G. Kennedy, M. A. A. Neil, and P. M. W. French, "Stimulated emission depletion microscopy with a supercontinuum source and fluorescence lifetime imaging," *Opt. Lett.* **33**(2), 113–115 (2008).
25. K. Weber, T. Bibring, and M. Osborn, "Specific visualization of tubulin-containing structures in tissue culture cells by immunofluorescence," *Exp. Cell Res.* **95**(1), 111–120 (1975).
26. C. A. Wurm, D. Neumann, R. Schmidt, A. Egner, and S. Jakobs, "Sample preparation for STED microscopy live cell imaging," D. B. Papkovsky, ed. (Humana Press, 2010), Chap. 11.
27. T. Staudt, A. Engler, E. Rittweger, B. Harke, J. Engelhardt, and S. W. Hell, "Far-field optical nanoscopy with reduced number of state transition cycles," *Opt. Express* **19**(6), 5644–5657 (2011).
28. B. Harke, J. Keller, C. K. Ullal, V. Westphal, A. Schönle, and S. W. Hell, "Resolution scaling in STED microscopy," *Opt. Express* **16**(6), 4154–4162 (2008).
29. D. Aquino, A. Schönle, C. Geisler, C. V. Middendorff, C. A. Wurm, Y. Okamura, T. Lang, S. W. Hell, and A. Egner, "Two-color nanoscopy of three-dimensional volumes by 4Pi detection of stochastically switched fluorophores," *Nat. Methods* **8**(4), 353–359 (2011).
30. J. Hotta, E. Fron, P. Dedecker, K. P. F. Janssen, C. Li, K. Müllen, B. Harke, J. Bückers, S. W. Hell, and J. Hofkens, "Spectroscopic rationale for efficient stimulated-emission depletion microscopy fluorophores," *J. Am. Chem. Soc.* **132**(14), 5021–5023 (2010).
31. G. Donnert, J. Keller, C. A. Wurm, S. O. Rizzoli, V. Westphal, A. Schönle, R. Jahn, S. Jakobs, C. Eggeling, and S. W. Hell, "Two-color far-field fluorescence nanoscopy," *Biophys. J.* **92**(8), L67–L69 (2007).
32. R. Schmidt, C. A. Wurm, S. Jakobs, J. Engelhardt, A. Egner, and S. W. Hell, "Spherical nanosized focal spot unravels the interior of cells," *Nat. Methods* **5**(6), 539–544 (2008).
33. J. Bückers, D. Wildanger, G. Vicidomini, L. Kastrop, and S. W. Hell, "Simultaneous multi-lifetime multi-color STED imaging for colocalization analyses," *Opt. Express* **19**(4), 3130–3143 (2011).
34. P. A. Pellett, X. Sun, T. J. Gould, J. E. Rothman, M.-Q. Xu, I. R. Corrêa, Jr., and J. Bewersdorf, "Two-color STED microscopy in living cells," *Biomed. Opt. Express* **2**(8), 2364–2371 (2011).
35. J. Tønnesen, F. Nadrigny, K. I. Willig, R. Wedlich-Söldner, and U. V. Nägerl, "Two-color STED microscopy of living synapses using a single laser-beam pair," *Biophys. J.* **101**(10), 2545–2552 (2011).
36. G. Vicidomini, R. Schmidt, A. Egner, S. W. Hell, and A. Schönle, "Automatic deconvolution in 4Pi-microscopy with variable phase," *Opt. Express* **18**(10), 10154–10167 (2010).
37. M. Yavuz and J. A. Fessler, "Statistical image reconstruction methods for randoms-precorrected PET scans," *Med. Image Anal.* **2**(4), 369–378 (1998).
38. M. Bertero, P. Boccacci, G. Desiderà, and G. Vicidomini, "Image deblurring with poisson data: From cells to galaxies," *Inverse Probl.* **25**(12), 123006 (2009).
39. G. Vicidomini, P. Boccacci, A. Diaspro, and M. Bertero, "Application of the split-gradient method to 3D image deconvolution in fluorescence microscopy," *J. Microsc.* **234**(1), 47–61 (2009).

1. Introduction

Providing non-invasive imaging of cells and tissue with molecular specificity, far-field fluorescence microscopy is one of the most powerful imaging modalities in biology. However, the spatial resolution of conventional far-field fluorescence microscopy is an order of magnitude poorer than the typical size of most relevant subcellular structures and organelles. Due to the far-field optical diffraction barrier [1], fluorophores emitting in the same wavelength λ_{em} range and observed through an objective lens of numerical aperture NA cannot be discerned if they are closer than $\lambda_{em}/(2NA)$. Likewise, diffraction makes it

impossible to focus excitation light of wavelength $\lambda_{\text{ex}} < \lambda_{\text{em}}$ more sharply than to a spot of $\lambda_{\text{ex}}/(2NA)$ in size. As a result, features that are spectrally identical and closer together than about this distance are difficult to separate. Since they absorb and emit together, the signal of these features will be confused. Current far-field fluorescence nanoscopy (superresolution) techniques overcome the diffraction resolution limit by precluding the simultaneous emission of adjacent spectrally identical fluorophores [2]. Individual techniques differ from each other by the molecular mechanism by which the fluorescence emission is precluded and by whether the emission takes place at i) controlled coordinates in space or ii) at random coordinates molecule by molecule [3, 4].

In stimulated emission depletion (STED) nanoscopy [5, 6], the coordinates at which fluorophores are allowed to emit is predefined by the so-called STED beam, which briefly turns off the capability of fluorophores to emit spontaneously. Because at least a single de-exciting photon must be available within the lifetime τ of the fluorescent excited-state, the focal intensity of the STED beam must exceed the threshold $I_s = h\nu_{\text{STED}}/(\sigma_{\text{STED}}\tau)$ which is the STED intensity at which the probability of stimulated emission equals the probability of spontaneous decay. $h\nu_{\text{STED}}$ denotes the STED photon energy and σ_{STED} is the cross-section for stimulated emission. The STED beam, usually formed as doughnut overlaid with the excitation beam, features a central zero-intensity point at which the fluorophores can still fluoresce. A doughnut crest intensity $I^{\text{m}}_{\text{STED}} \gg I_s$ ensures that fluorescence emission is possible only in a narrow range $d \approx \lambda_{\text{ex}}/(2NA(1 + a I^{\text{m}}_{\text{STED}}/I_s)^{1/2})$ around the central zero-intensity point, where the prefactor a used here depends on the STED implementation and considers the temporal and spatial properties of the particular STED beam (see Material and Methods). Translating the beams across the sample and recording the fluorescence yields images with sub-diffraction resolution d .

As τ is of the order of 10^{-9} s and σ_{STED} of the order of 10^{-16} cm², attaining sub-diffraction resolution requires $I^{\text{m}}_{\text{STED}} \approx 0.1\text{--}1$ GW cm⁻². Depending on the wavelength, intensities of this order can still be live-cell compatible [7–10], yet variants of STED operating at lower light intensities are preferred because they may provide a higher resolution in (living) cells and because of practical aspects such as the availability of lasers. A route to low light intensity operation is to replace STED with a different fluorescence modulation mechanism, e.g. by transferring the fluorophore transiently to a generic dark (triplet) state [11, 12], or to a long-lived conformational state [13–15]. However, since they usually involve atom relocations, the switching kinetics of these alternative fluorescence switching mechanisms cannot be as fast as those induced by the nearly instant transition of stimulated emission [15]. For all these reasons, STED nanoscopy remains highly attractive.

Continuous-wave STED (CW-STED) versions reduce the instantaneous (peak) intensity request of the STED beam by up to about 10-fold compared to pulsed STED (P-STED) implementations [16]. However, due to the lower CW-STED intensity, early fluorescence photons emitted right after the excitation of molecules and coming from the outer part of the excitation area drastically reduce the imaging contrast [17]. Recently, it has been demonstrated that this problem can be solved using a pulsed excitation and a time-gated detection to discard unwanted early photons [18, 19]. Nevertheless, although CW-STED implementation with time-gated detection provides sharp images with comparatively low STED beam intensity, the STED beam time-averaged power is higher than in the pulsed implementation.

An unswerving approach to reduce the demand for both the peak intensity and the average power is to increase the relevant stimulated emission cross-section σ_{STED} . The spectral dependence of σ_{STED} follows, in a first approximation, the emission spectrum of the fluorophore in use [20, 21]. Therefore, choosing a STED wavelength close to the emission maximum would result in a higher efficiency for the stimulated emission process. However, due to the non-negligible overlap of the emission and excitation spectra, the probability to excite the molecule directly with the STED beam is also increased, resulting in undesired

'background' fluorescence and reduced imaging contrast. For this reason, at present, STED nanoscopy uses STED wavelengths within the far-red edge of the emission spectrum of a fluorophore. The origin of this background fluorescence is mainly anti-Stokes excitation (AStEx). AStEx is assumed to primarily reflect the Boltzmann distributed thermal occupation of higher vibrational states within the electronic ground state S_0 . For these states the energy gap to the S_1 is smaller, making the transition $S_0 \rightarrow S_1$ by absorption of a red-shifted STED beam photon more probable.

According to Boltzmann, a linear reduction of the temperature reduces the occupation of higher vibrational states exponentially and thereby also the AStEx. Therefore a STED nanoscope working at liquid nitrogen temperature has been examined [22]. This study has shown that AStEx is substantially reduced and STED wavelengths with larger stimulated emission cross-section are readily applicable. However, low temperature solutions require substantial technical efforts and are not compatible with live-cell imaging.

Here, we propose a method that allows substantial AStEx by the STED beam, but eliminates the effects of the fluorescence signal associated with it. If AStEx is non-negligible, the STED image consists of the standard sub-diffraction image generated by the excitation beam, plus a low-resolution 'background' image due to AStEx [23]. Given a sufficient signal-to-noise ratio (SNR) and a faithful separate recording of the background image, the high-resolution image can be unveiled by subtraction. Providing a method that is able to faithfully remove the AStEx fluorescence background allows relaxing the STED wavelength constraint and thus reduces the required STED intensity by harnessing a larger stimulated emission cross-section.

2. Materials and methods

Determination of the AStEx signal

The fluorescence signal induced by the excitation beam has the same wavelength spectrum as the AStEx background. However, high-frequency interruption of the excitation beam with respect to the STED beam helps to single out the desired signal. To quantify the AStEx induced background, we divide the measurement in two equal time-intervals: i) the "close" interval (or "close" phase), when only the doughnut-shaped STED beam is applied and only fluorescence induced by the AStEx of the STED beam is collected and ii) the "open" interval (or "open" phase), when both beams are applied and fluorescence induced by both the STED and the excitation beams are collected. The signal detected in the "close" phase is used to measure the AStEx background signal and is subtracted from the "open" phase signal to retrieve the signal induced by the excitation beam only (synchronous photon counting or photon counting in 'lock-in' mode). By iterating the procedure pixel by pixel, the AStEx background image is subtracted from the raw STED image data and the sub-diffraction STED image is faithfully recovered.

In the case of a pulsed excitation, the "close" and "open" phases are readily obtained by dividing the inter-pulse intervals into two time-gates, as shown in Fig. 1(a) and (b), and by choosing appropriate repetition rates for the excitation and the STED beams, such that during the "close" phase fluorescence induced only by the STED beam is detected. In an implementation using a CW-STED beam (Fig. 1(a)), a pulsed excitation beam with repetition rate $f_{\text{exc}} < (-2\ln(0.01)\tau)^{-1}$ ensures that the probability to collect fluorescence induced by the excitation beam in the second half of the excitation pulse interval is negligible (<1%). Since the excited-state lifetime τ of a typical fluorophore is ~2-3 ns, we used a repetition rate $f_{\text{exc}} = 40$ MHz. For the all-pulsed implementation (Fig. 1(b)), the pulsed STED and excitation lasers operated in a master-slave configuration: we synchronized the excitation laser at half of the repetition rate of the STED laser, i.e. $f_{\text{exc}} = f_{\text{STED}}/2$. Again, $f_{\text{STED}} < (-\ln(0.01)\tau)^{-1}$ ensures that in the second half of the excitation pulse interval only fluorescence induced by the STED beam (AStEx) is collected. In our scheme, a repetition rate of $f_{\text{STED}} = 76$ MHz or 71.4 MHz for the

STED beam satisfied these conditions. Note that the two time-gates have the same width and the proposed approach can be easily combined with the gated STED (gSTED) implementation [18, 19, 24] by starting the Gate1 with a time-delay T_g from the excitation pulse.

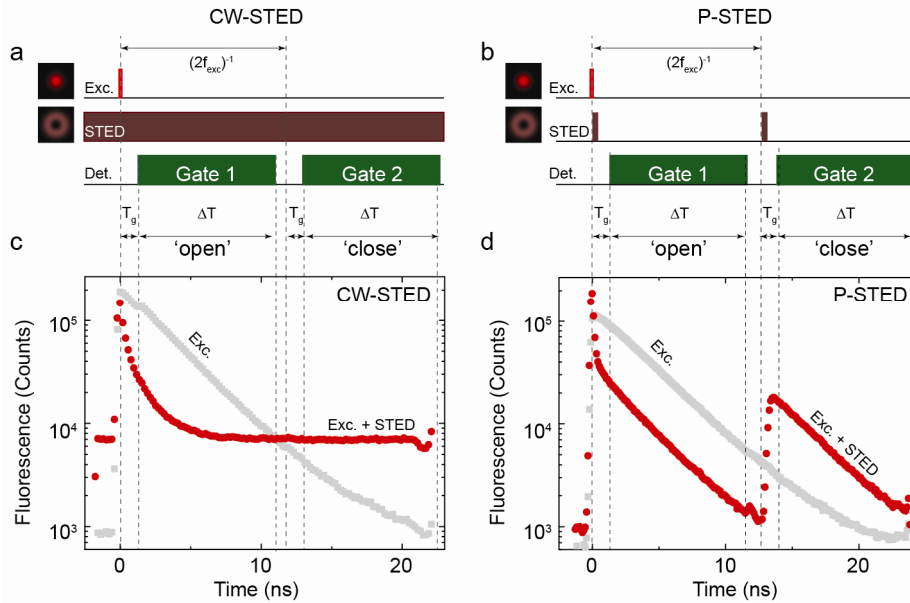


Fig. 1. Principle of the anti-Stokes excitation (AStEx) determination. (a,b) Experimental time sequence for (a) CW-STED and (b) P-STED implementations. The AStEx contribution is taken from the signal detected during Gate 2. Time-correlated single-photon counting histograms in log-scale of ATTO-647N labeled microtubules in PtK2 cells for (c) CW-STED and (d) P-STED configurations. For comparison, time-correlated single-photons histograms generated just by the excitation beam, i.e. without the STED beam, are also shown (gray lines).

Figure 1(c) shows the photon arrival-times histogram from fluorescence of ATTO-647N labeled microtubules imaged with CW-STED. The CW nature of the STED beam obviously generates a uniform background across the whole pulse time-interval, while the low repetition rate of the pulsed excitation beam ensures that fluorescence induced by the STED beam dominates the signal of the second half of the pulse interval (compare gray and red lines in the second half of the pulse period). For the pulsed STED implementation (Fig. 1(d)), the photon arrival-times histogram clearly shows the overlapping of two separate decay distributions. The second decay is induced almost solely by the STED beam and lies completely in the second half of the excitation pulse period.

Sample preparation

The mammalian PtK2 cell line was grown as described previously [25]. Cells were seeded on standard glass coverslips to a confluence of about 80% and fixed with ice-cold methanol (-20°C) for 4 min followed by an incubation in blocking buffer (PBS containing 1% BSA). Microtubules and vimentin filaments were stained using an immunofluorescence labeling protocol [26] involving a primary antibody (anti-vimentin mouse IgG [V9] or anti β -tubulin mouse IgG (monoclonal), Sigma, Saint Louis, MO) and a secondary antibody (sheep anti-mouse IgG, Dianova, Hamburg, Germany) labeled with the dyes ATTO-647N, ATTO-565, or ATTO-Rho12. Both antibodies were diluted in blocking buffer and incubated for 1 h each followed by several washings in blocking buffer. Preparations were embedded in Mowiol (with DABCO).

STED setup

Experiments were performed on two home-built STED microscopes similar to those described previously [19, 27]. The first setup was used to image ATTO-647N labeled samples. The setup featured a 635 nm pulsed diode laser (LDH-D-C-635, PicoQuant, Berlin, Germany) for excitation (repetition rate from single shot to 80 MHz) and a Ti:Sapphire laser (Mira900, Coherent, Santa Clara, CA) tuned to the wavelengths 730 and 760 nm and operating either in continuous-wave (CW) or pulsed mode (repetition rate 76 MHz) for CW- or P-STED, respectively. In the later case, the excitation pulses were synchronized to the STED pulses which were stretched to ≈ 250 ps by two glass rods and a 120 m long polarization maintaining single mode fiber (AMS Technology, München, Germany). Excitation and STED beams were overlapped and separated from the fluorescence by two custom-made dichroic mirrors (AHF Analysentechnik, Tübingen, Germany) and directed toward the objective lens (HCX PL APO 100 \times /1.40–0.7 Oil, Leica Microsystems, Wetzlar, Germany). The fluorescence was detected by the same objective lens, cleaned up with appropriate bandpass filters and injected into a multimode optical fiber with an opening corresponding to about the Airy disc of the fluorescence light. The fiber was attached to a single-photon-counting module (id100-MMF50, id Quantique, Carouge, Switzerland) connected to a time-correlated-single-photon-counting (TCSPC) board (SPC-730, Becker & Hickl GmbH, Berlin, Germany). Image acquisition was performed by scanning the sample with a 3D piezo stage (NanoMax TS 3-axis, Thorlabs GmbH Europe, Dachau, Germany). Photon arrival-time information provided by the TCSPC board was used to sort out the signal into the “open” and “close” time-intervals.

The second setup imaged Atto565 and AttoRho12-stained samples. Excitation at 532 nm was realized using a pulsed laser diode (PicoTA, Picoquant) which were synchronized with 71.4 MHz STED pulses at 647 nm, generated by an actively mode locked (APE, Berlin, Germany) Ar-Kr laser (Spectra Physics-Division of Newport Corporation, Irvine, USA). The beams were combined using acousto-optical tunable filters (AOTF) (Crystal Technologies, Palo Alto, USA) and coupled into a microscope (DMI 4000B with an objective lens ACS APO 63x/1.3NA, Leica Microsystems) equipped with a three-axis piezo stage scanner (PI, Karlsruhe, Germany) which also imaged the fluorescence signal onto a confocally arranged aperture of a photon counting module (SPCM-AQR-13-FC, PerkinElmer, Canada). The AOTFs also served as fast shutters and independent power controllers for each laser beam as well as a filter system selecting the fluorescence signal. For additional filtering, an appropriate band-pass filter was used. For the second setup the “close” and “open” time-intervals were obtained using two home-built electronic gates, which simply separated the fluorescence photons gathered during the according intervals. This is a much simpler and more cost-effective implementation than the TCSPC implemented in the first setup.

In both setups the STED focal doughnuts were created by introducing polymeric phase plates (RPC Photonics, Rochester, NY) applying a helical phase ramp of $\exp(i\varphi)$, with $0 < \varphi < 2\pi$ in the STED beams. The helical phase distribution was imaged into the back aperture of the objective lens. Excitation lasers were synchronized to the STED lasers by home-built electronic delay lines and frequency divider units. The STED and confocal reference images were recorded nearly simultaneously on a line-by-line basis by opening and closing a shutter placed in the STED beam path. Note that the image produced just by the STED beam is not a reference confocal image, because of the STED beam's doughnut shape.

Intensity and power measurements

For both the STED and excitation light, the average power $\langle P \rangle$ was measured at the back aperture of the objective lens. The average STED intensity at the doughnut crest can be estimated by $\langle I \rangle_{STED} = k \langle P \rangle_{STED} / A_{STED}$ where A_{STED} denotes the STED focal area of the diffraction limited Gaussian spot and $k = 0.3$ is a scaling factor taking into account the larger

area of the doughnut. We determined $A_{STED} \approx \pi (\text{FWHM}_{STED} / 2)^2$ from the full-width at half-maximum (FWHM_{STED}) of the diffraction limited Gaussian spot. The values of $\text{FWHM}_{STED} \approx 350$ nm ($\lambda_{STED} = 760$ nm) and $\text{FWHM}_{STED} \approx 340$ nm ($\lambda_{STED} = 730$ nm) were measured by imaging a gold bead of sub-diffraction diameter (80 nm gold colloid, EmGC80, BBInternational, Cardiff, UK) in a non-confocal mode. For the CW STED beam the peak intensity is identical with the time-averaged intensity, $I_{STED} = \langle \dot{I}_{STED} \rangle$, while for the pulsed STED beam (with assumed rectangular pulses), the peak intensity I_{STED} relates to the average intensity $\langle \dot{I}_{STED} \rangle$ by $I_{STED} = \langle \dot{I}_{STED} \rangle T / T_{STED}$, with T denoting the period between two pulses, i.e. the inverse of the repetition rate f_{STED} , ($T = 1/f_{STED}$), and T_{STED} being the pulse width.

Threshold intensity analysis

The saturation or fluorescence off-switching threshold intensity I_s is determined from the analysis of the fluorescence intensity profiles (full-width at half-maximum; FWHM) of many stained microtubules as a function of the STED peak intensity at the doughnut crest I_{STED}^m . Applying a scalar focusing theory [19], the fluorescence intensity profile generated by a point-like object imaged by a STED nanoscope, i.e the radial profile of the effective point-spread-function (E-PSF), can be approximated by a Gaussian function with a FWHM equaling to

$$FWHM_{gP} = d_c \sqrt{1 + d_c^2 \beta (I_{STED}^m / I_s) T_{STED} / (\ln(2) \tau)} \quad (1)$$

for the gP-STED implementation with time-gated detection (fluorescence signal is collected after the STED pulse) and

$$FWHM_{gCW} = d_c \sqrt{1 + d_c^2 \beta (I_{STED}^m / I_s) (1 + T_g / (\ln(2) \tau))} \quad (2)$$

for the gCW-STED implementation with time-gated detection (the fluorescence signal is collected after a time-delay T_g from the excitation pulse). Here d_c denotes the FWHM of the confocal PSF, β is a constant that depends on the shape of the doughnut STED beam [28], the threshold STED intensity I_s at which the probability of stimulated emission equals the probability of spontaneous decay, τ the fluorescence lifetime of the fluorophore, and T_{STED} the width of the STED pulse.

Another fact which has to be taken into account is that microtubules cannot be considered as point-like objects. In particular, when labeled with secondary antibodies, the typical diameter of the fluorescent structure reaches 50-70 nm [29]. Hence, the measured microtubule image profile is given by the convolution of the Gaussian E-PSF and the cross-section of the microtubular construct. To derive an analytical function describing the microtubule intensity profile we approximated the cross-section of the microtubular construct with a Gaussian function. The new equation reads

$$FWHM_{mt} = \sqrt{FWHM_{gP/gCW}^2 + s^2} \quad (3)$$

with s denoting the FWHM of the Gaussian-like cross-section of the construct. For our experiments we assumed $s = 50$ nm.

3. Results

Following our experimental configuration (Fig. 1), we used the time-gate 1 in the first half of the pulse interval to generate the raw STED image (“open” phase) and the time-gate 2 in the second half to estimate the AStEx background image (“close” phase). Using these two images we recovered the final superresolution image simply by subtracting the AStEx background image from the raw STED image. Since the low-resolution background image and the raw

STED image are obtained (quasi-) simultaneously, potential bleaching and/or drifting effects have been inherently taken into account.

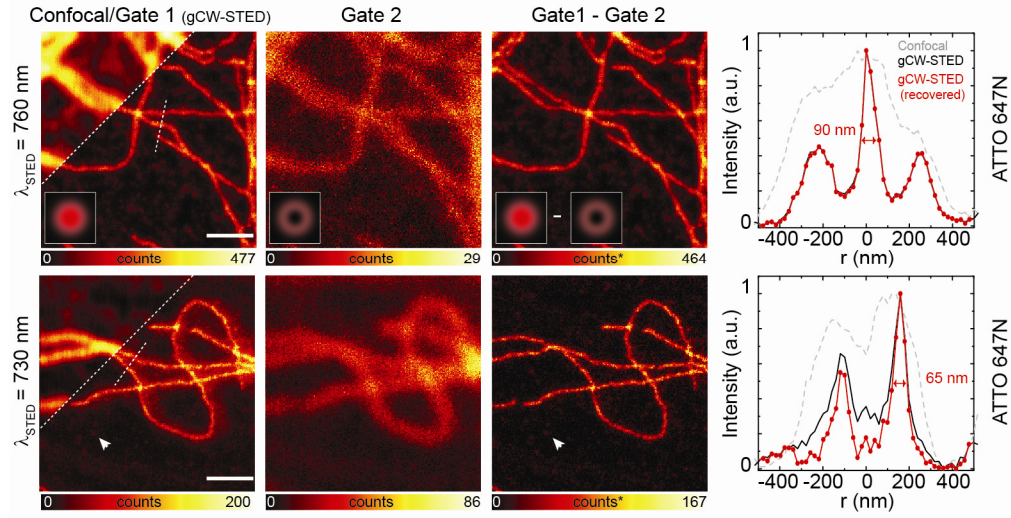


Fig. 2. Comparison of CW-STED nanoscopy operating at $\lambda_{\text{STED}} = 760$ nm (upper panels) and 730 nm (lower panels): confocal (top left corners), raw gCW-STED (Gate1, left panels), anti Stokes excitation (AStEx) induced fluorescence generated by the STED beam (Gate 2, middle left panels) and recovered gCW-STED images (Gate1 – Gate2, middle right panels) of ATTO-647N labeled microtubules as well as normalized intensity profiles along the dashed lines (right panels). The asterisk in the color look-up table denotes that the negative counts obtained after subtraction are clipped to zero. Excitation: $\lambda_{\text{ex}} = 635$ nm, $f_{\text{ex}} = 40$ MHz and $\dot{a}P_{\text{ex}} \bar{n} = 5$ μ W; STED: $\dot{a}P_{\text{STED}} \bar{n} = 290$ mW at $\lambda_{\text{STED}} = 760$ nm and $\dot{a}P_{\text{STED}} \bar{n} = 250$ mW at 730 nm; time-gated detection: $T_{\text{g}} = 1$ ns and $\Delta T = 8$ ns; Pixel size 20 nm; Pixel dwell-time 0.5 ms. In this and the following figures, the inserted focal excitation spots and doughnuts are symbolic and not to scale. Scale bars: 1 μ m.

Figures 2 and 3 show the results obtained using our approach on ATTO-647N labeled microtubules for gCW-STED and gP-STED implementations, respectively. As expected from the fluorescence emission spectrum of ATTO-647N (compare inset Fig. 4(a)), AStEx at $\lambda_{\text{STED}} = 760$ nm was negligible (upper middle panels). Consequently, no significant improvement has been obtained (compare upper left panels with upper right panels). However, at $\lambda_{\text{STED}} = 730$ nm AStEx was not negligible anymore (low-middle panels); in fact, it drastically reduced the contrast of the STED images (low-left panels). Note that for a safe comparison the raw STED images (left panels) are obtained by collecting photons in the first time-gate only. Importantly, the sub-diffraction STED images are fully recovered using our approach (lower right panels). In addition, the dim structures in the raw STED image (indicated by white arrows) are conserved in the final image. This is because our approach is not just the application of an arbitrary threshold to the raw STED data, rather it fully considers the different contributions to the fluorescence signal in space at nearly identical time points.

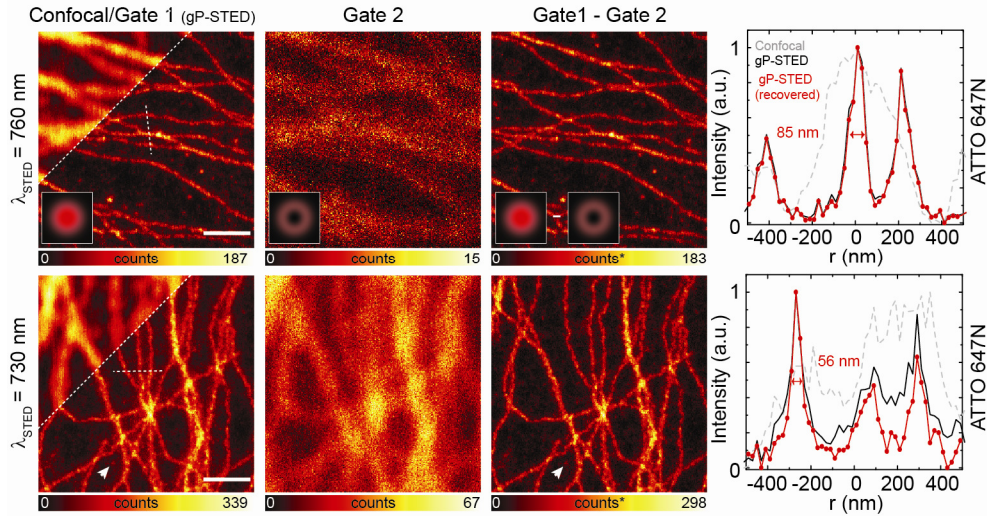


Fig. 3. Comparison of pulsed STED nanoscopy at $\lambda_{\text{STED}} = 760$ nm (upper panels) and $\lambda_{\text{STED}} = 730$ nm (lower panels). The figure depicts confocal (top left corners), raw gP-STED (Gate1, left panels), AStEx by the STED beam (Gate2, middle left panels) and recovered gP-STED images (Gate1- Gate2, middle right panels) of ATTO-647N labeled microtubules as well as normalized intensity profiles along the dashed lines (right panels). The asterisk denotes that negative counts following subtraction are clipped to zero. Excitation: $\lambda_{\text{ex}} = 635$ nm, $f_{\text{ex}} = 76/2$ MHz and $\hat{a}P_{\text{ex}} \bar{n} = 5 \mu\text{W}$; STED: $f_{\text{STED}} = 76$ MHz, $\hat{a}P_{\text{STED}} \bar{n} = 70$ mW at $\lambda_{\text{STED}} = 760$ nm and $\hat{a}P_{\text{STED}} \bar{n} = 60$ mW at $\lambda_{\text{STED}} = 730$ nm; time-gated detection: $T_{\text{g}} = 1$ ns and $\Delta T = 8$ ns; Pixel size 20 nm; Pixel dwell-time 0.5 ms. Scale bars: 1 μm .

The ATTO-647N emission spectra suggest a 2-3 fold increase of the stimulated cross-section when the STED wavelength is reduced from $\lambda_{\text{STED}} = 760$ nm to $\lambda_{\text{STED}} = 730$ nm (inset Fig. 2). To demonstrate that the intensity required to achieve the desired resolution decreases, we imaged ATTO-647N labeled microtubules for different STED powers. Figure 4 plots the FWHM of the intensity profile through microtubules as a function of the focal average power of the STED beam and its instantaneous intensity for the gCW-STED (Fig. 4(a)) and gP-STED (Fig. 4(b)) implementations. Most importantly, in both configurations, the STED intensity required to reach a certain FWHM decreased for the shorter wavelength. For example, a FWHM < 100 nm has been achieved with approximately 3-times lower peak intensity at 730 nm compared to 760 nm STED light. The FWHM reduction for the CW-STED implementation can be described by Eq. (3) with $I_s = 11.7 \pm 0.7$ MW/cm² and 4.2 ± 0.3 MW/cm² for $\lambda_{\text{STED}} = 760$ nm and 730 nm, respectively. This confirms a ~ 2 -3 fold increase of the utilized effective stimulated emission cross-section from $\sigma_{\text{STED}} = 0.7 \pm 0.04 \times 10^{-16}$ cm² for 760 nm to $\sigma_{\text{STED}} = 2.1 \pm 0.2 \times 10^{-16}$ for 730 nm.

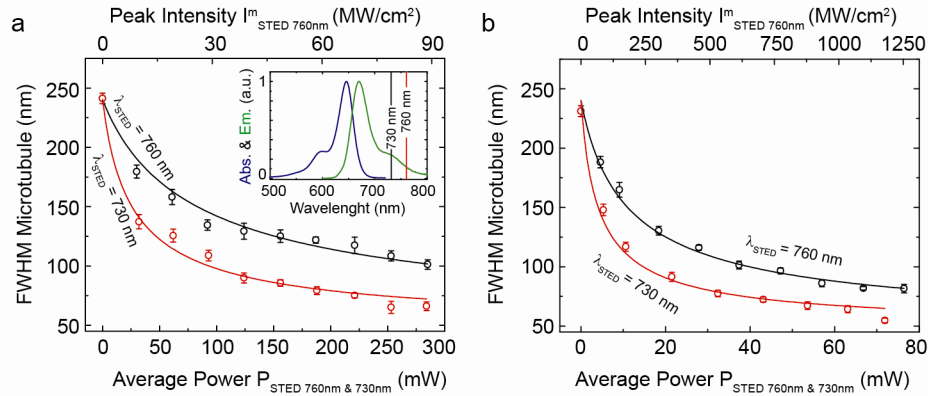


Fig. 4. Dependence of the FWHM determined from STED images of ATTO-647N-labeled microtubules on the average STED power for (a) the CW-STED and (b) the pulsed STED configuration (mean \pm s.e.m.; $n = 10$). Solid lines show theoretical fits of Eq. (3) to the data with $d_c = 235$ nm, $\beta = 1.04 \cdot 10^{-5}$ nm $^{-2}$, $\tau = 3.15$ ns, $s = 50$ nm, $T_g = 1$ ns and $T_{\text{STED}} = 250$ ps. The inset in (a) shows the absorption (blue) and emission (green) spectra of the fluorophore ATTO-647N and the applied STED wavelengths. Note that the time averaged power of the STED beam was measured before entering the lens. Due to losses in the lens, the power at the sample is actually lower by 30% and 25% at 760 nm and 730 nm, respectively.

We observed a similar increase for the P-STED implementation; the FWHM data recorded with gP-STED can also be well described by Eq. (3) with $I_s = 7.2 \pm 0.3$ MW/cm 2 ($\sigma_{\text{STED}} = 1.2 \pm 0.05 \times 10^{-16}$ cm 2) for $\lambda_{\text{STED}} = 760$ nm and $I_s = 2.9 \pm 0.3$ MW/cm 2 ($\sigma_{\text{STED}} = 3.1 \pm 0.3 \times 10^{-16}$ cm 2) for $\lambda_{\text{STED}} = 730$ nm. For the same STED wavelength, slightly different I_s and effective stimulated cross-sections σ_{STED} have been estimated from the CW-STED and P-STED implementation; these differences are likely due to differences in the experimental approach and also due to the simplified model of the dye applied here, neglecting excitation to higher states [10, 30]. For example the spectra of the STED beam for CW and pulsed implementations are different. Short pulses are characterized by broad spectrum (about 7 nm in width), while the spectrum of the CW STED light is much narrower (< 1 nm), resulting in slightly different cross-sections.

While our approach can be used to optimize the STED wavelength for a specific fluorophore, it also increases the number of suitable dyes for a given STED wavelength. Figure 5 compares the images of vimentin filaments labeled with two spectrally distinct dyes, ATTO-565 and ATTO-Rho12, obtained using a pulsed STED beam at $\lambda_{\text{STED}} = 647$ nm. $\lambda_{\text{STED}} = 647$ nm is routinely used for the dye ATTO 565 [16]. Still, the image contrast is degraded due to a weak AStEx contribution. Our method restores the contrast nearly completely. On the other hand, $\lambda_{\text{STED}} = 647$ nm induces a substantial fluorescence signal for the dye ATTO-Rho12, which features a ~ 10 nm red-shifted excitation spectrum with respect to ATTO-565. The image recorded for ATTO-Rho12 is strongly degraded by AStEx. As a consequence, the background signal is comparable to the fluorescence signal from the excitation beam. Yet our approach recovers the sub-diffraction image. Thus, for the red-shifted dye, the applied laser intensity can be used more effectively; half of the intensity of STED light is sufficient for ATTO-Rho12 in order to render the sub-diffraction resolution image comparable to ATTO-565. The increase in number of available dyes for a given STED wavelength will certainly widen the options for implementing multi-color STED microscopy schemes [31–35].

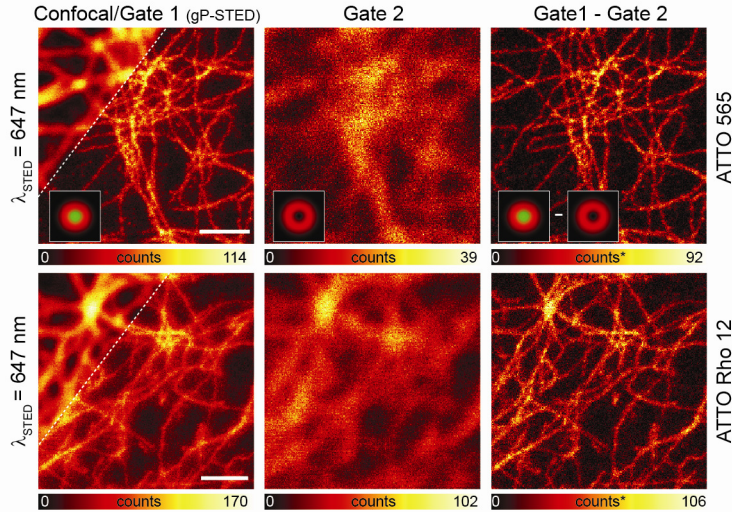


Fig. 5. Comparison of gP-STED nanoscopy imaging obtained with two spectrally different fluorophores, ATTO-565 (upper panels) and ATTO-Rho12 (lower panels), using the same excitation and STED beams. The figure depicts confocal (top left corners), raw gP-STED (Gate1, left panels), AStEx induced fluorescence from the STED beam (Gate2, middle panels) and recovered gP-STED images (Gate1 – Gate2, right panels) of labeled vimentin filaments. Excitation: $\lambda_{\text{ex}} = 532 \text{ nm}$, $f_{\text{ex}} = 35.7 \text{ MHz}$ and $\dot{a}P_{\text{ex}}\tilde{n} = 1 \mu\text{W}$; STED: $\lambda_{\text{STED}} = 647 \text{ nm}$, $f_{\text{STED}} = 71.4 \text{ MHz}$, for ATTO Rho12 $\dot{a}P_{\text{STED}}\tilde{n} = 35 \text{ mW}$; for ATTO-565 $\dot{a}P_{\text{STED}}\tilde{n} = 78 \text{ mW}$ time-gated detection: $T_{\text{e}} = 0.1 \text{ ns}$ and $\Delta T = 10 \text{ ns}$; Pixel size 19 nm ; Pixel dwell-time $100 \mu\text{s}$. Scale bars: $1 \mu\text{m}$.

4. Discussion and conclusion

Blue-shifting the STED beam towards the emission maximum of the fluorophore reduces the intensity required to obtain images with a given sub-diffraction resolution. In the experiments reported in this study, the reduction amounted to a factor of up to three when blue-shifting the STED wavelength by 30 nm. The fluorescence background stemming from the anti-Stokes excitation of the fluorophore by the STED beam is recorded in a temporally interlaced measurement and subtracted. The method is applied to both CW and pulsed STED configurations, and can be elegantly combined with the recently demonstrated gated version of CW STED microscopy. Clearly, our approach can also be implemented with CW excitation if the excitation beam is periodically interrupted in order to generate the “open” and “close” phase signals. Other implementations for determining the anti-Stokes excitation background can also be conceived. For example, one can use a bidirectional fast beam scanning scheme, in which the forward and backward scans are registered separately, with the excitation beam turned on for one scan direction only.

As usual, the efficiency of the method is ultimately limited by the signal-to-noise ratio (SNR). Here, we obtained the number of fluorescent photons representing the final image (N_{FEX} , i.e. the one stemming from the molecules at the doughnut center) by subtracting the AStEx photons (N_{ASStEx}) from the total signal. To avoid differences between the independently measured background and the background contribution to the total signal (other than shot noise), the “open” and “close” phases were measured quasi-simultaneously. Namely, in our approach the high-frequency ($\sim 40 \text{ MHz}$) interruption of the excitation beam cancels out much of the undesired signal fluctuations stemming from laser output instabilities, bleaching, drifting, and other factors. The desired fluorescent signal can be recovered if $N_{\text{FEX}} > \sqrt{(N_{\text{FEX}} + 2N_{\text{ASStEx}})}$, or equivalently if the $\text{SNR} = N_{\text{FEX}}/\sqrt{(N_{\text{FEX}} + 2N_{\text{ASStEx}})}$ of the subtracted signal is > 1 . Furthermore, note that (i) N_{ASStEx} stems from a different and in fact larger area since it is produced by the doughnut-shaped STED beam; (ii) in case of CW-STED $f_{\text{exc}} < 40 \text{ MHz}$

increases only N_{AStEx} but not N_{FEX} ; (iii) the desired SNR and the upper bound $f_{\text{exc}} < (-2\ln(0.01)\tau)^{-1}$ determine the pixel integration time of our method.

The necessity of increasing the acquisition time to maintain a suitable SNR can be reduced by substituting the subtraction method with more sophisticated statistical image restoration methods, such as maximum likelihood estimation (MLE). For example one could consider jointly estimating both the sub-diffraction and the ASStEx mean (noiseless) images from the two shot noise limited (Poissonian) time-gated raw images [36]. Alternatively, one could estimate the sub-diffraction mean image directly from the subtraction of the two raw images. However, since the distribution of the subtracted image is not Poisson distributed anymore, suitable approximations of the log-likelihood have to be used to derive reliable MLE algorithms [37]. Finally, since both time-gated images can be written as a convolution of the specimen with a suitable point-spread function, one could combine deconvolution [38, 39] and MLE frameworks to restore the specimen fluorophore distribution. On the other hand, the iterative nature of the statistical image restoration algorithms and the request of *a-priori* information virtually preclude the ability to render the superresolution images online as is the case with our simple subtraction approach.

In conclusion, while our method comes at a comparatively small expense of increased acquisition time, it substantially enlarges the versatility of STED nanoscopy; in particular it greatly simplifies the implementation of multi-color imaging schemes with a single STED wavelength.

Acknowledgments

The authors acknowledge Volker Westphal for the design of the electronic delay lines. We thank Rebecca Medda and Ellen Rothermel for preparing the samples and Andreas Schönle for the software Inspector.